Energy & Environmental Science

ROYAL SOCIETY OF CHEMISTRY

PAPER

View Article Online
View Journal | View Issue

Cite this: *Energy Environ. Sci.*, 2023, **16**, 5904

Kinetic pathways of fast lithium transport in solid electrolyte interphases with discrete inorganic components†

Yikang Yu, ‡[ab] Hyeongjun Koh,‡[c] Zisheng Zhang, ‡[e] Zhenzhen Yang,[d] Anastassia N. Alexandrova, [ef] Mangilal Agarwal,[a] Eric A. Stach *[c] and Jian Xie *[a]

Received 22nd June 2023,
Accepted 11th October 2023

DOI: 10.1039/d3ee02048g

rsc.li/ees

The transport of lithium ions in the solid electrolyte interphase (SEI) has been previously accepted to proceed in two steps: a fast pore diffusion through the outer, porous organic layer followed by a slow knock-off or vacancy diffusion in the inner, dense inorganic layer. The second step is believed to be the rate-limiting step during fast-charging. In this study, we have intentionally constructed a thicker SEI (SEI-rich) structure on the surface of monoclinic Nb_2O_5 (H-Nb_2O_5) by adding $LiNO_3$ into a conventional ethylene carbonate based electrolyte. The electrochemical performance of two electrodes, one SEI-rich and one with few SEI (SEI-lean), was found to be almost the same, including their fast-charging capability and cycling stability, despite the significant difference in their SEI structure. Importantly, analysis using cryogenic scanning/transmission electron microscopy showed the discrete decoration of individual inorganic particles (*e.g.*, Li_2O) and amorphous species (LiN_xO_y/organic components) over the surface of H-Nb_2O_5. These discrete inorganic particles are in contradiction to the formation of dense inner inorganic layer, which has been commonly postulated. Based on these findings, we propose a new mechanism for Li ion transport through the SEI: one-step pore diffusion, without the second step slow diffusion. This one-step pore diffusion process provides an extremely fast Li ion transport, and effectively removes the kinetic limitation of Li ion transport in the SEI for fast charging. These results strongly suggest that the influence of SEI structure on the transport kinetics of lithium ions is much less significant than previously accepted. These results offer a new understanding of possible lithium ion transport pathway within SEI and may have implications for the future designs of fast-charging battery materials.

Broader context

The elucidation of the Li transport pathway in solid electrolyte interphase is crucial for the rational design of lithium ion batteries anode with fast-charging capability. However, the existing two-step mechanism consisting of a fast pore diffusion in the outer porous organic layer and a slow knock-off or vacancy diffusion in the inner dense inorganic layer, fails to adequately explain lots of unconventional Li transport behaviors such as the Li-solvent co-intercalation into the graphite. It suggests the likely existence of other Li transport pathway within the SEI layer. In this article, a one-step fast pore diffusion mechanism is revealed in SEI-rich H-Nb_2O_5 with discrete inorganic particles. This new understanding of the Li diffusion mechanism in this intercalation H-Nb_2O_5 material may also have referential value to those low voltage anode materials with SEI-rich structures such as graphite, and offer implications for the future designs of fast-charging battery materials.

[a] *Department of Mechanical and Energy Engineering, Purdue School of Engineering and Technology, Indiana University – Purdue University Indianapolis, Indianapolis, IN, 46202, USA. E-mail: jianxie@iupui.edu, stach@seas.upenn.edu*
[b] *School of Mechanical Engineering, Purdue University, West Lafayette, IN, 47907, USA*
[c] *Department of Materials Science and Engineering and Laboratory for Research on the Structure of Matter, University of Pennsylvania, Philadelphia, PA, 19104, USA*
[d] *Chemical Sciences and Engineering Division, Argonne National Laboratory, Lemont, IL, 60439, USA*
[e] *Department of Chemistry and Biochemistry, Los Angeles, CA, 90095, USA*
[f] *California NanoSystems Institute, University of California, Los Angeles, Los Angeles, CA, 90095, USA*
† Electronic supplementary information (ESI) available. See DOI: https://doi.org/10.1039/d3ee02048g
‡ These authors contributed equally to this work.

1. Introduction

The solid electrolyte interphase (SEI) – a protective layer formed from the electrolyte decomposition on the anode surface during the initial operation of lithium ion batteries (LIBs) – has a critical impact on cycle life, rate capability and safety.[1–3] The SEI allows for the transport of lithium ions while also maintaining electronic isolation that prevents further electrolyte decomposition. The widely accepted picture of the SEI is that it consists of two layers: a porous outer layer composed of organic components (*e.g.*, dilithium ethylene dicarbonate, and ROLi, *etc.*), and an dense inner layer of inorganic materials such as Li_2O, Li_2CO_3, and LiF.[1,4,5] Compared to Li ion diffusion within the solid phase of the host materials (*e.g.* graphite), the diffusion of lithium ions through the SEI is believed to have a much higher activation energy barrier.[6] Significant efforts have been made in recent decades to understand the mechanisms of Li diffusion across the SEI, and a two-step mechanism has been proposed. This mechanism involves an extremely rapid pore diffusion through the porous organic outer layer, followed by a knock-off or vacancy diffusion in the dense inorganic (*e.g.* Li_2CO_3) inner layer.[7,8] The presence of the SEI affects the rate at which lithium ions can diffuse through the anode, with faster diffusion typically occurring through the porous outer organic layer and slower diffusion occurring through the dense inner inorganic layer. In this regard, the second, slow diffusion process through the dense SEI inorganic layer ultimately limits the fast-charging capability of the battery materials. Therefore, most reported anode materials capable of fast-charging, such as Nb_2O_5, TiO_2, and $Nb_{16}W_5O_{55}$, are typically operated at relatively high potentials ($\geq$0.8 V *vs.* Li^+/Li), which effectively suppresses the decomposition of the electrolyte components and forms a thinner SEI structure (refer as ''SEI-lean'').[9–14] This SEI-lean structure may allow for direct intercalation of lithium ions into the host material, (*i.e.*, diffusion through the SEI layer is not required), potentially improving the high-rate performance of the battery.[15–17]

Great advances have been made in improving fast-charging performance through the rational design of the SEI components that facilitate fast ion transport, based on the long-held picture described above.[18–20] However, the observations of SEI-rich structures on $Li_4Ti_5O_{12}$ (LTO) due to its high catalytic activity and the recent discovery of low potential ($<$0.5 V *vs.* Li^+/Li) materials such as $Li_3V_2O_5$ and black phosphorus that exhibit fast-charging capabilities appear to challenge this established mechanism.[21–23] This raises the question whether the presence of SEI-rich structure necessarily impedes the rapid Li ion diffusion through SEI, and consequently, fast Li (de)intercalation capability. Moreover, the large energy barrier associated with desolvation and crossing the SEI processes have traditionally been recognized as the primary limiting factors, contributing to the sluggish kinetics in graphite anode.[6,24] However, those findings demonstrating the fast-charging capability of graphite anodes through a solvent co-intercalation mechanism along with a wide range of alkali metal ions (*e.g.*, Li^+, Na^+, K^+),[25–29] strongly suggest the existence of an alternative Li transport pathway within SEI layer. This pathway enables graphite, which is typically considered ''sluggish kinetics'', to exhibit high rate capability. Furthermore, the phenomenon of solvent molecules co-intercalation with Li ions into graphite has been observed even in conventional SEI layers generated from carbonate-based electrolyte (1.0 M $LiPF_6$ in ethyl carbonate/dimethyl carbonate). Previously, it was believed that these stable SEI layers allowed for reversible Li ion transport solely without accompanying solvent molecules intercalation.[30] The established two-step mechanism fails to adequately explain these unconventional Li transport behaviors in graphite anode and SEI-rich anode materials, suggesting the likely existence of fast Li diffusion mechanism without stripping solvent molecules across the entire SEI layer. Thus, it becomes essential to examine the fast-charging behaviors in these SEI-rich structures, as there could be an alternative Li transport mechanism capable of fast Li ion transport.

In this study, an SEI-rich structure on the surface of an H-Nb_2O_5 anode is intentionally created by adding $LiNO_3$ to an ethylene carbonate (EC) based electrolyte, in which $LiNO_3$ can be easily reduced ($>$1.5 V *vs.* Li^+/Li). This creates an artificially fabricated SEI-rich structure despite the high operation potential of H-Nb_2O_5.[31,32] In contrast, use of a neat, conventional EC-based electrolyte without $LiNO_3$ additives leads to a very thin SEI on the H-Nb_2O_5 anode because of the high stability of this electrolyte above 1.0 V (*vs.* Li^+/Li). H-Nb_2O_5 may serve as a SEI-lean anode with very little SEI. We observed that these two H-Nb_2O_5 anodes exhibited almost the same high-rate performance independent of their SEI structures. Subsequently, we correlated the corresponding electrochemical response with the spatial distribution of the organic and inorganic components in the SEI using cryogenic scanning/transmission electron microscopy (cryo-S/TEM). It has been found that individual Li_2O nanocrystallites and amorphous LiN_xO_y species are formed in the SEI-rich structure, and these discrete Li_2O particles do not form a dense inorganic layer. Our findings strongly suggest that the fast Li ion transport and cycling stability of H-Nb_2O_5 are not significantly affected by either the inorganic components or the thickness of the SEI. These results indicate that Li transport through the SEI occurs *via* a one-step pore diffusion mechanism. Namely, the formation of discrete inorganic particles in an amorphous matrix allows Li diffusion to bypass these inorganic particles, eliminating the second slower solid-state diffusion process. Lithium diffusion *via* the one-step pore diffusion mechanism is much faster than Li ion diffusion within the H-Nb_2O_5 particle itself, which can remove the kinetic limitation of Li ion transport across the entire SEI-rich structure to realize fast-charging.

2. Results and discussion

2.1 SEI fabrication and characterization

One of the reasons why certain anode materials, such as Nb_2O_5, TiO_2, $Nb_{16}W_5O_{55}$, $CrNb_{11}O_{29}$, exhibit superior rate performance is due to their ''SEI lean'' structure, resulting from their high

operating potentials (Fig. 1(a), $\geq$0.8 V *vs.* Li^+/Li).[9–14] In this potential range, the electrolyte tends to be stable, and the formation of SEI is suppressed due to the limited electrolyte decomposition. For example, EC-based electrolyte, widely used in LIBs, forms an SEI layer below 0.9 V (*vs.* Li^+/Li).[33] This suggests that the transport of Li ions in the SEI layer may restrict the fast (de)intercalation of Li ions within the anode host materials during high-rate operation. To illustrate an explicit SEI effect on high-rate capability of the anode materials, we have chosen to study typical fast-charging material, H-Nb_2O_5, cycled in two different electrolytes: a neat EC-based electrolyte (1.2 M $LiPF_6$ in mixture of ethylene carbonate and ethylene methyl carbonate) and a EC-based electrolyte with an $LiNO_3$ additive ($\sim$0.01 M). Since the H-Nb_2O_5 operates at a high potential range (1.0–3.0 V *vs.* Li^+/Li), the former electrolyte is designated as "SEI lean", while the latter is designated as "SEI-rich" due to the higher reduction potential of the $LiNO_3$ ($>$1.5 V *vs.* Li^+/Li).[31,34] To validate if such a "SEI-rich" structure was created, a low rate (C/4) discharge and charge combined with cyclic voltammetry (CV) experiments were conducted, as the low rate facilitates SEI formation. As shown in Fig. 1(b), the initial Coulombic efficiency (ICE) decreased from 95.0% to 87.3% with $LiNO_3$ additives, accompanied by an increased initial discharge capacity from 203.4 mA h g^{-1} to 221.4 mA h g^{-1}, but with a similar charge capacity ($\sim$194 mA h g^{-1}). A new cathodic peak appears at $\sim$1.85 V (*vs.* Li^+/Li) on the CV curves (Fig. S1, ESI†) apart from the Li intercalation peak at $\sim$1.40 V (*vs.* Li^+/Li), suggesting that the decomposition of $LiNO_3$ accounts for the increased initial discharge capacity. To further exclude the presence of a side reaction between $LiNO_3$ and H-Nb_2O_5, a linear sweep voltammetry (LSV) measurement was conducted using a Li|Cu half-cell with the same scan rate (0.5 mV s^{-1}). The cathodic reduction of $LiNO_3$ starts at $\sim$1.50 V (*vs.* Li^+/Li), while no cathodic peak is observed for the neat EC-based electrolyte (Fig. 1(c)), which is consistent with previous reports.[31] The discrepancy between the LSV and CV cathodic peak position may be due to catalytic effects of the electrode materials (*e.g.*, Nb_2O_5, Super P). These results confirm that an SEI-rich structure is intentionally formed on the H-Nb_2O_5 due to the addition of $LiNO_3$ additives.

X-ray photoelectron spectroscopy (XPS) was utilized to analyze the surface composition of H-Nb_2O_5 after the initial cycle. The H-Nb_2O_5 electrodes cycled in EC-based electrolyte have a strong signal from the LiF inorganic component, as evidenced by the Li 1s ($\sim$55.5 eV) and F 1s spectra (684.6 eV) shown in Fig. 2(a) and (b). However, it should be noted that the high intensity of the sodium carboxymethyl cellulose (CMC) binder from the C 1s spectra made it difficult to infer the organic components of the SEI in both samples (Fig. 2(d) and (h)).[36] In contrast, an additional peak located at $\sim$400.2 eV for the N 1s spectra is present in those H-Nb_2O_5 anodes cycled in the $LiNO_3$

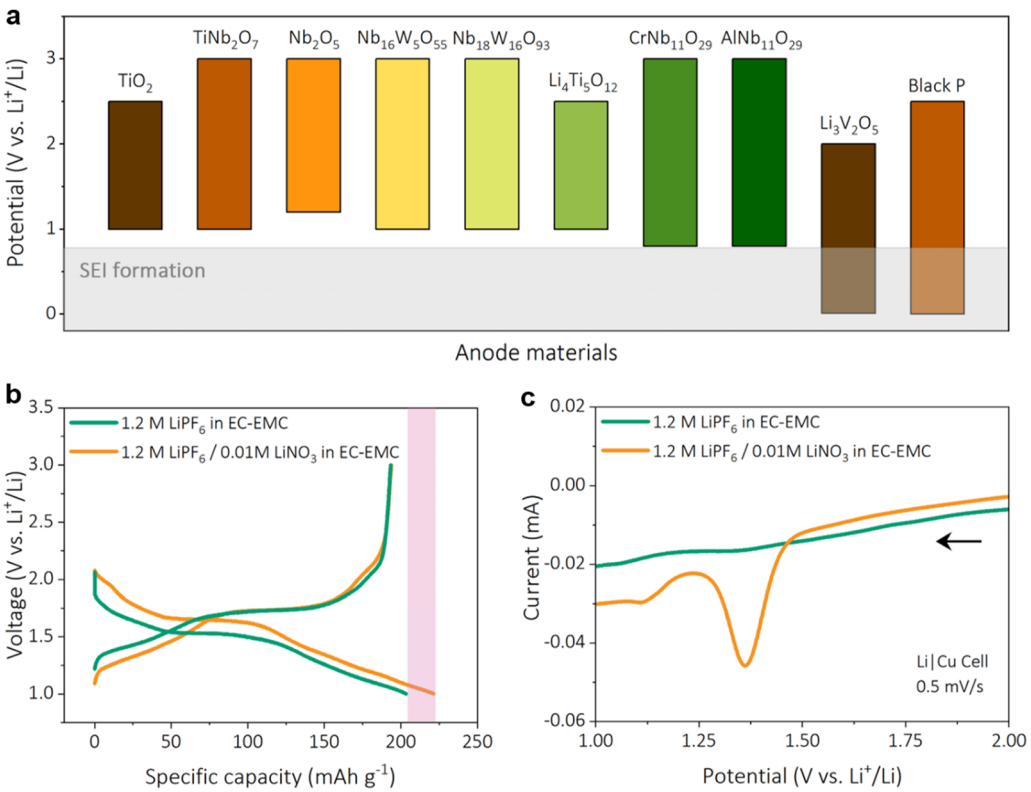

Fig. 1 Design of SEI layers on H-Nb_2O_5. (a) Operating potential (*vs.* Li^+/Li) range of typical anode materials capable of fast-charging, based on previous reports.[9–14,22,23,35] (b) Initial charge and discharge (C/4 rate) curves for H-Nb_2O_5 with neat EC-based electrolyte and $LiNO_3$-added EC-based electrolyte. (c) Linear sweep voltammetry (0.5 mV s^{-1}) of Li|Cu cells with neat EC-based electrolyte and $LiNO_3$ added EC-based electrolyte, indicating SEI formation with $LiNO_3$ decomposition.

added electrolyte (Fig. 2(g)), in addition to the LiF components (Fig. 2(e) and (f)), corresponding to a lithium nitrogen species (LiN_xO_y).[31,37] However, there is no N 1s signal detected in the SEI-lean H-Nb_2O_5 samples (Fig. 2(c)). Compared to the SEI formed from the neat $LiNO_3$-free EC-based electrolyte with the sole LiF inorganic component, the nitrogen species originated from the reduction of $LiNO_3$ in the SEI-rich structure on Nb_2O_5 surface, leading to the observed ICE decrease (Fig. 1(b)).

The surface composition obtained from XPS reveals a broad range of chemical components. However, this information does not provide any spatially resolved information due to the large probe size, as most of these SEIs do not directly attach to Nb_2O_5 particles (refer as indirect SEI) but distribute across the whole electrode. Consequently, the above XPS results cannot describe the spatial distribution of the different components in the SEI, and thus makes interpretation of the lithium ion diffusion mechanism difficult.[38] To determine the spatial distribution of the various components, we further utilized cryogenic scanning/transmission electron microscopy (cryo-S/TEM) to study the SEI that directly attach to the Nb_2O_5 particles (refer as direct SEI), which is highly relevant to the Li (de)intercalation kinetics into the host materials. The SEI components, which are composed of inorganic and organics decomposition products, are chemically reactive and sensitive to the electron beam at room temperature, but they remain intact at cryogenic condition.[39,40]

Cryo-TEM was used to visualize the SEI that adhered to the Nb_2O_5 particles cycled in the two different electrolytes. The two SEIs were found to be porous but were different in thickness and compositions. It was observed that the both SEIs on the particles did not fully cover the Nb_2O_5 particles but the coverage of the SEI on the Nb_2O_5 cycled in $LiNO_3$ added EC-based electrolyte was significantly higher than that in the electrolyte without $LiNO_3$ (Fig. S3, ESI†). The components of these dense SEI layers were further examined using high resolution cryo-TEM (HRTEM). The SEI regions from both Nb_2O_5 particles cycled in neat EC-based electrolyte and Nb_2O_5 particles in $LiNO_3$ added EC-based electrolyte are shown in Fig. 3(a)–(c) and (f)–(h), respectively. The light contrast regions outside the particle are an indicator of SEI, which is typically composed of light elements such as Li, C, and O. In contrast, the Nb_2O_5 particles exhibit dark contrast because of the constituents with the high atomic number of Nb. Both Nb_2O_5 particles cycled in the neat EC-based electrolyte and in the $LiNO_3$ added EC-based electrolyte display a distinct region where a SEI layer does not exist (Fig. 3(b), (g) and Fig. S4c, d, g and h, ESI†). However, their overall distributions of the direct SEI are different in thickness. The thin SEI layer (<10 nm, Fig. S4a and b, ESI†) on these H-Nb_2O_5 particles cycled in neat EC-based electrolyte suggests the slight reduction of the electrolyte components (*e.g.*, $LiPF_6$, EC, EMC), consistent with the XPS results (Fig. 2(a) and (b)). In contrast, thicker SEI regions (20–40 nm, Fig. 3(f) and Fig. S4e, f, ESI†) were observed with $LiNO_3$ additives due to the preferential reduction of NO_3^-. Fig. 3(d) and (e) displays HRTEM images of the direct SEI layer constructed in neat EC-based electrolyte with a SEI-lean structure. The fast Fourier Transform (FFT)

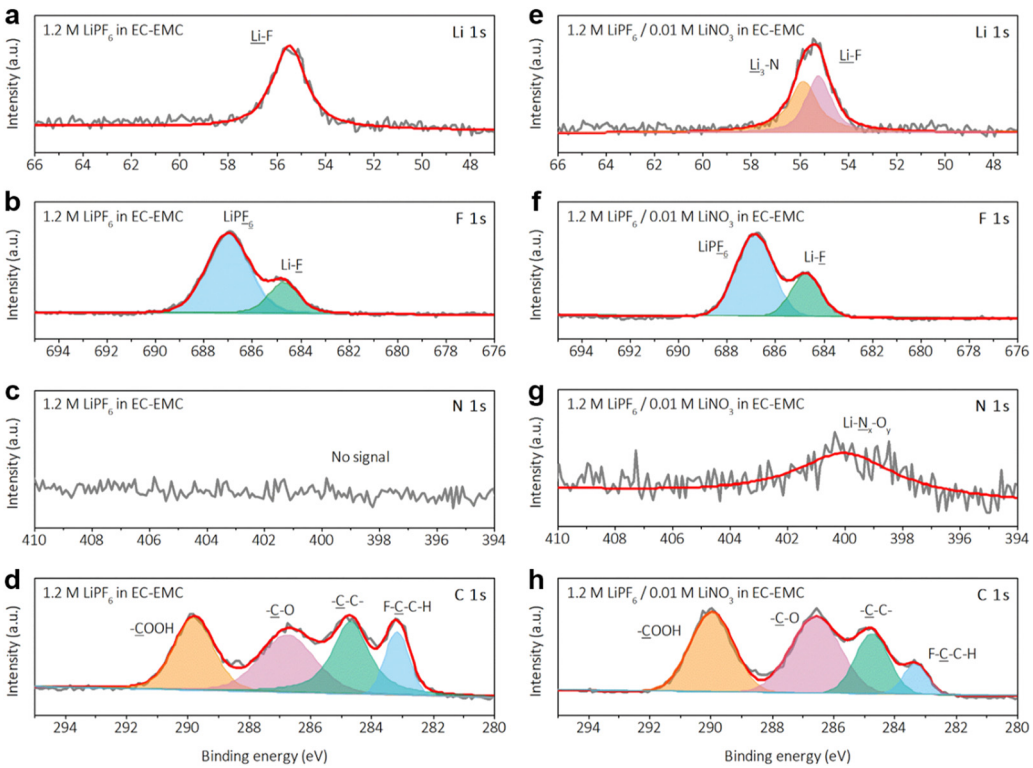

Fig. 2 Indirect SEI information obtained by XPS measurement on H-Nb_2O_5 after initial cycle. (a)–(d) Li 1s, F 1s, N 1s, and C 1s spectra acquired by H-Nb_2O_5 cycled in neat EC-based electrolyte. (e)–(h) Li 1s, F 1s, N 1s, and C 1s spectra acquired by H-Nb_2O_5 cycled in $LiNO_3$ added EC-based electrolyte.

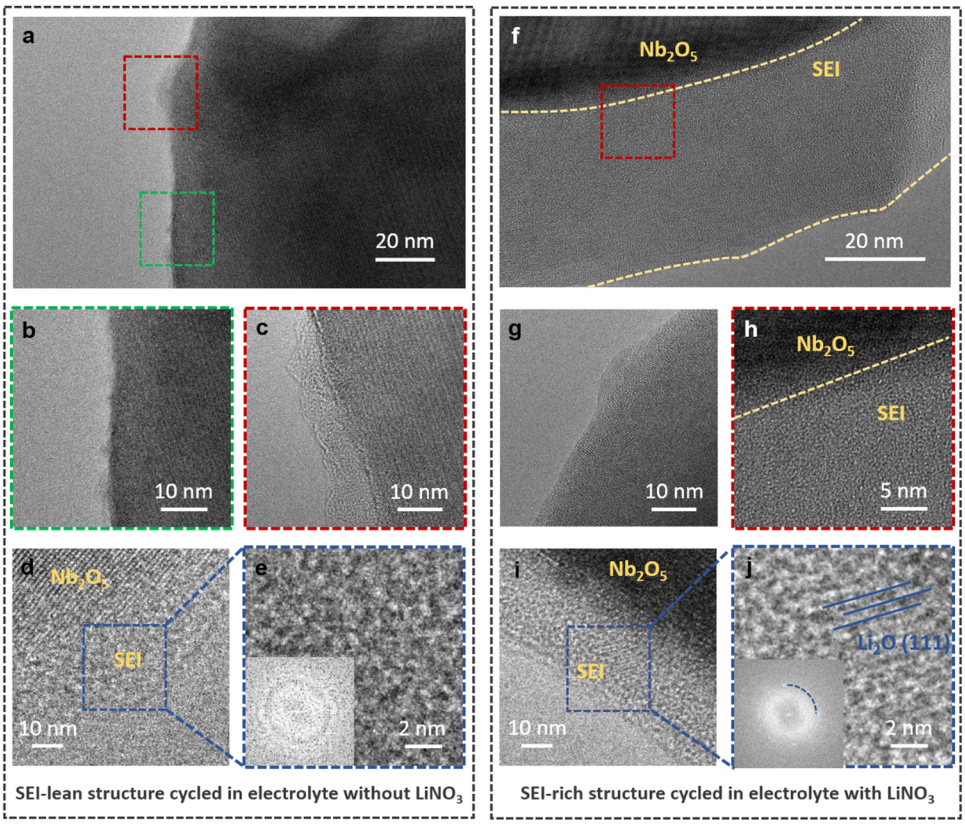

Fig. 3 Direct SEI information obtained by cryo-TEM on H-Nb_2O_5 after the initial cycle. (a)–(e) cryo-TEM images of H-Nb_2O_5 cycled in neat EC-based electrolyte. The boxed region in green and red indicates the electrode surface is covered (b) without and (c) with SEI, respectively. (d) A HRTEM image of the direct SEI region (e) from a magnified image of the boxed region in blue (d). Inset image is the FFT result of the corresponding image. (f)–(j) cryo-TEM images of H-Nb_2O_5 cycled in $LiNO_3$ added EC-based electrolyte. The electrode surface (g) without SEI and (h) with SEI, which is a magnified image in red box from (f). (i) A HRTEM image of the direct SEI on the electrode and a magnified image (j) of the region in blue from (i). The inset shows the FFT pattern of the boxed region in blue and the line in the quad circle shows (111) reflection of Li_2O.

pattern in Fig. 3(e) shows a highly amorphous structure. More cryo-TEM observations from different regions (Fig. S5a and b, ESI†) further confirm that the SEI formed from neat EC-based electrolyte is highly amorphous. On the other hand, the presence of $LiNO_3$ reduction in the electrolyte gives rise to the formation of discrete Li_2O nanoparticles in the direct SEI (Fig. 3(i), (j), and Fig. S5c, d, ESI†) while there is no LiF particle identified in the same region based on HRTEM. In addition to the cryo-TEM results, the direct SEI structures were also visualized using scanning electron microscopy (SEM). SEM images show a similar morphology on these micro-sized H-Nb_2O_5 (2–5 μm) with smooth surfaces, in which there is no obvious SEI structure visible (Fig. S2, ESI†) due to the low resolution of SEM. Further energy dispersive X-ray spectroscopy (EDS) was conducted on these particle surfaces, which reveals that the atomic percentage of oxygen element is greatly increased from ~33% to ~46% with $LiNO_3$ additives (Fig. S6, ESI†). It is in accordance with oxygen-rich (Li_2O) direct SEI structure (Fig. 3(i) and Fig. S5c, d, ESI†). However, the element concentration obtained from XPS shows a limited difference (~2%) of oxygen atomic percentage on electrode surface (Table S1, ESI†) but a discrepancy of nitrogen concentration (~1% with $LiNO_3$ and ~0% without $LiNO_3$). The different results from XPS and SEM EDS further suggest that the direct SEI (information revealed by SEM EDS) constitute a limited portion of the components across the whole electrode (indirect SEI, information revealed by XPS) thus, an oxygen-rich direct SEI plays a negligible influence on the oxygen percentage of the broad SEI structure detected by XPS.

In addition to the images of HRTEM, cryo-EELS elemental mapping was conducted to distinguish the distribution of SEI components in the two samples (Fig. 4). The cryo-EELS mapping suggests that C and O signals are rich in SEI structure of both Nb_2O_5 samples cycled in EC-based electrolyte with or without $LiNO_3$ (Fig. 4(a), (b), (e) and (f)) while the presence of Nb_2O_5 is evidenced by EELS signals of Nb M_3-edge and O K-edge signals (Fig. 4(b), (c), (f) and (g)). However, the SEI rich in carbon and oxygen from neat EC-based electrolyte does not fully surround the Nb_2O_5 particle while the SEI showing carbon and oxygen signals from $LiNO_3$ added EC-based electrolyte covers the surface of the electrode, which is consistent with the cryo-TEM images shown in Fig. 3. Carbon and oxygen components originate from the organic components by slight reduction of EC and ethylene methyl carbonate (EMC) solvent. The cryo-EELS elemental maps further reveal clear N signal from the direct SEI layer in the H-Nb_2O_5 cycled with $LiNO_3$

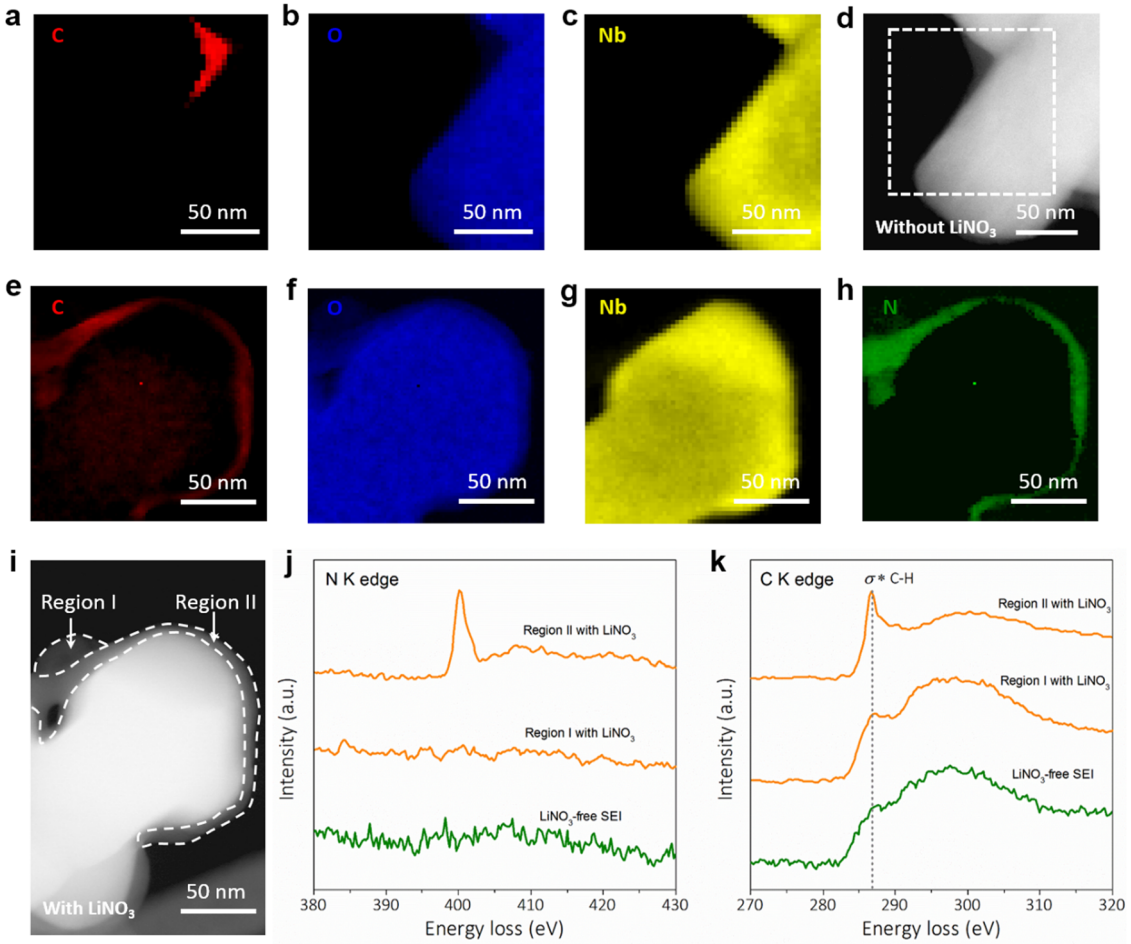

Fig. 4 Cryogenic electron energy loss spectroscopy (cryo-EELS) elemental maps (carbon K-edge, oxygen K-edge, niobium M_3-edge, and nitrogen K-edge) of direct SEI structures from H-Nb_2O_5 cycled in neat EC-based electrolyte (a)–(c) and $LiNO_3$ added EC-based electrolyte (e)–(h) from a selected area of high-angle angular dark field (HAADF) cryo-STEM image (d) and (i), respectively. (j) and (k) EELS spectra of N K-edge and C K-edge from these SEI structures at different regions as marked region I and region II in (i).

additives (Fig. 4(h)). Furthermore, the EELS spectra of the N K-edge feature with a peak located at ~400.0 eV (Fig. 4(j), region II), which matches with the Li–N–O spectra.[41] This observation confirms the presence of amorphous LiN_xO_y species in the direct SEI decomposed from $LiNO_3$. Moreover, the C K-edge as shown in Fig. 4(k) has a characteristic peak located at ~288 eV that corresponds to C–H bonding.[42] The intensity of the C–H bonding peak is greatly suppressed from the SEI structure decomposed from EC-based electrolyte (Fig. 4(k), $LiNO_3$-free SEI). These results strongly suggest that a complete decomposition of electrolyte to carbonate based components (*e.g.*, Li_2CO_3, dilithium ethylene dicarbonate) is suppressed with $LiNO_3$ additives and that more components with C–H bonding (*e.g.*, ROLi) form. However, there is an SEI region (region I in Fig. 4(i)) from SEI-rich structure demonstrates a similar chemical species with those SEI-lean structures according to the EELS N K-edge and C K-edge spectra (Fig. 4(j) and (k)). The appearance of this region on the outmost SEI region (region I) may be due to the depletion of $LiNO_3$ in the electrolyte during the charge and discharge process. The difference between region I and region II was further investigated using the EELS O K-edge and Li K-edge spectra (Fig. S7, ESI†). The fingerprints for the 1s to π* transition of the C=O group or N and O bonding (~533 eV, Fig. S7a, ESI†) were observed from region I to region II according to the O K-edge spectra.[43] The Li K-edge spectra at region I demonstrate a typical $LiPF_6$ characteristic with two peaks located at ~62 eV and ~70 eV,[44] which is consistent with the XPS results. However, region II exhibits slightly different results, with a different position for Li K-edge spectra observed. The thicker SEI (position 1, Fig. S7c, ESI†) shows a Li_2O characteristics with the fingerprint-peaks located at ~56 eV and ~62 eV.[44] The slight shift of the peak location between position 1 and 2 may be attributed to the transition from Li_2O (position 1) to LiN_xO_y species (position 2). The EELS and XPS results, in combination, show that the direct SEI structure is composed of LiN_xO_y and crystallized Li_2O that arise from $LiNO_3$ additives. Combined with the TEM observation in Fig. 3, the crystallized Li_2O nanoparticles are decorated on the inner direct SEI structure discretely, while the insoluble LiN_xO_y species disperse in the

direct SEI as an amorphous form. In particular, the LiF species found by the XPS have not been discovered in the compact SEI layer in both samples. Therefore, the LiF tends to precipitate out across the electrode surface and constitutes the indirect SEI.

The stability of as-formed SEI layer was further investigated after 200 cycles at 10C using cryo-(S)TEM. Even after 200 cycles, those Nb_2O_5 particles cycled in the neat EC-based electrolyte keep their SEI-lean structure and the clean surfaces were found in most of the areas (Fig. S8, ESI†). Moreover, the most edge regions at the Nb_2O_5 particles lack carbon K-edge EELS signal (Fig. S8d–g, ESI†), suggesting that the SEI-lean condition is maintained after the long-term cycling. These observations confirm the high stability of the EC-based electrolyte in a high operation potential range (1.0–3.0 V, *vs.* Li^+/Li). In contrast, the thickness of the SEI-rich structure on those Nb_2O_5 particles cycled in $LiNO_3$ added electrolyte is decreased from ~40 nm (Fig. 3(f) and Fig. S4e, f, ESI†) to less than ~20 nm (Fig. S9, ESI†) after long term cycling. We found that the nitrogen K-edge EELS signal (Fig. S9a–f, ESI†) disappeared after 200 cycles, suggesting that $LiNO_3$ was depleted in the electrolyte and the as-formed LiN_xO_y was decomposed, which results in the reduction on the SEI layer thickness. The reduction of $LiNO_3$ leads to the formation of radicals that are able to participate in the electrolyte decomposition until the depletion of $LiNO_3$.[45] As a result, even after the fully decomposition of the LiN_xO_y, thicker SEI was maintained after long-term cycling compared to those Nb_2O_5 particles cycled in neat EC-based electrolyte. Most importantly, further HRTEM and FFT characterizations (Fig. S9j, ESI†) demonstrate a discrete decoration of the individual Li_2O particles over the amorphous SEI layer, showing that the features of the SEI-rich structure still maintained after 200 cycles despite a thickness reduction. Thus, we conclude that both as-formed SEIs from the neat EC-based electrolyte and that from the $LiNO_3$ added electrolyte have a high stability to study their Li diffusion mechanism.

2.2 High rate performance and cycling stability.

To correlate the SEI structure with the electrochemical response, a series of electrochemical characterizations were conducted including C-rate, long time galvanostatic charge/discharge cycles, and electrochemical impedance spectra (EIS). It was found that the Nb_2O_5 exhibits a much larger specific capacity among different C-rates in the neat EC-based electrolyte (Fig. S10, ESI†) than that in $LiNO_3$ added electrolyte for early cycles (~30 cycles). Based on this finding, one may draw the conclusion that a SEI-lean structure with less components are beneficial for the battery materials performance, which is consistent with recent reports for a graphite anode.[46] Moreover, it suggests that the transport of Li ions across the SEI may limit the kinetics of the whole lithium (de)intercalation process as previously reported.[47] However, this capacity difference became negligible (<3%) with extended cycling numbers at both 1C and 10C rates (Fig. 5(a)). For the long-term cycling process at both 1C and 10C rate, the specific capacity of H-Nb_2O_5 increases first and then stabilizes in a small range independent of the SEI structures. We assign these beginning cycles with increase of capacity as activation cycles, as indicated in Fig. 5(a), which is a common phenomenon in H-Nb_2O_5 materials.[48,49] Moreover, Nb_2O_5 cycled in both electrolytes show an ultra-stable (~500 cycles at 1C, ~1000 cycles at 10C) electrochemical cycling performance with small capacity decay except a different length of activation cycles. During low rate cycling (1C), both samples only require nearly 50 cycles for the activation (Fig. S11, ESI†). However, much longer activation cycles (~200 cycles) are observed with SEI-rich structure at the high rate condition (10C, Fig. 5(a)) compared to a SEI-lean structure (~50 cycles) as indicated by the activation cycle (Fig. 5(b) and (c)). These intriguing findings corroborate that the SEI structure (*e.g.*, thickness, inorganic components) has a very limited effect on fast-charging capability, such as specific capacity and cycling stability in our cases. In other words, the Li transport across the SEI regions does not limit the kinetics of Li (de)intercalation process for H-Nb_2O_5 even at 10C-rate. It is worth noting that we used Li metal foils as a reference electrode to investigate the electrochemical performances of Nb_2O_5. $LiNO_3$ additives in electrolytes have been widely used to improve the performance of Li metal anode by lowering its overpotential and forming a stable SEI.[50] As a result, to exclude the positive effect of $LiNO_3$ additives on Li metal anode in Nb_2O_5/Li half-cells, the Li–Li symmetrical cells were constructed and evaluated. However, the Li plating/striping voltage profiles in a Li–Li symmetrical cell at different current density (from 0.1 mA cm^{-2} to 2.0 mA cm^{-2}) demonstrate a similar overpotential no matter if there is $LiNO_3$ or not (Fig. S12, ESI†). Therefore, it confirms that a limited amount $LiNO_3$ additives (~0.01 M) has a negligible effect on Li metal anode, while half-cell performance is dominated by the Nb_2O_5 surface structures.

2.3 One-step pore diffusion in SEI

To further explain these findings, the comparison of Li diffusion coefficients (D_{Li^+}) from certain anode materials and SEI components is listed in Table S2 (ESI†). According to previous molecular dynamics calculations and experimental results, the Li ion diffusion coefficient (D_{Li^+}) *via* inorganic SEI components (*e.g.* Li_2O, LiF, Li_2CO_3) and organic components (*e.g.* dilithium ethylene dicarbonate) has a magnitude of 10^{-14} cm s^{-1}, which is much lower than those that of the anode materials (*e.g.* Nb_2O_5, 7.547×10^{-13} cm^2 s^{-1}).[51–53] Based on this information, the second step of the solid-state diffusion through these inorganic components (*e.g.* Li_2O) or possible organic components (*e.g.*, dilithium ethylene dicarbonate) in the inner dense SEI layer would be much slower than the lithium diffusion in the Nb_2O_5 materials itself if a typical two-step diffusion mechanism took place.[7] However, the SEI-rich structure does not pose a diffusion barrier for fast-charging even at 10C rate charge/discharge, which contradicts the typical two-step mechanism (Fig. 6(e)). The discrete decoration of inorganic particles (Li_2O) over the H-Nb_2O_5 surface in the thick organic layer allows this pore diffusion across the entire SEI layer without the lithium ion being required to diffuse through these inorganic particles. Thus, one step pore diffusion of lithium ions (Fig. 6(f)) through

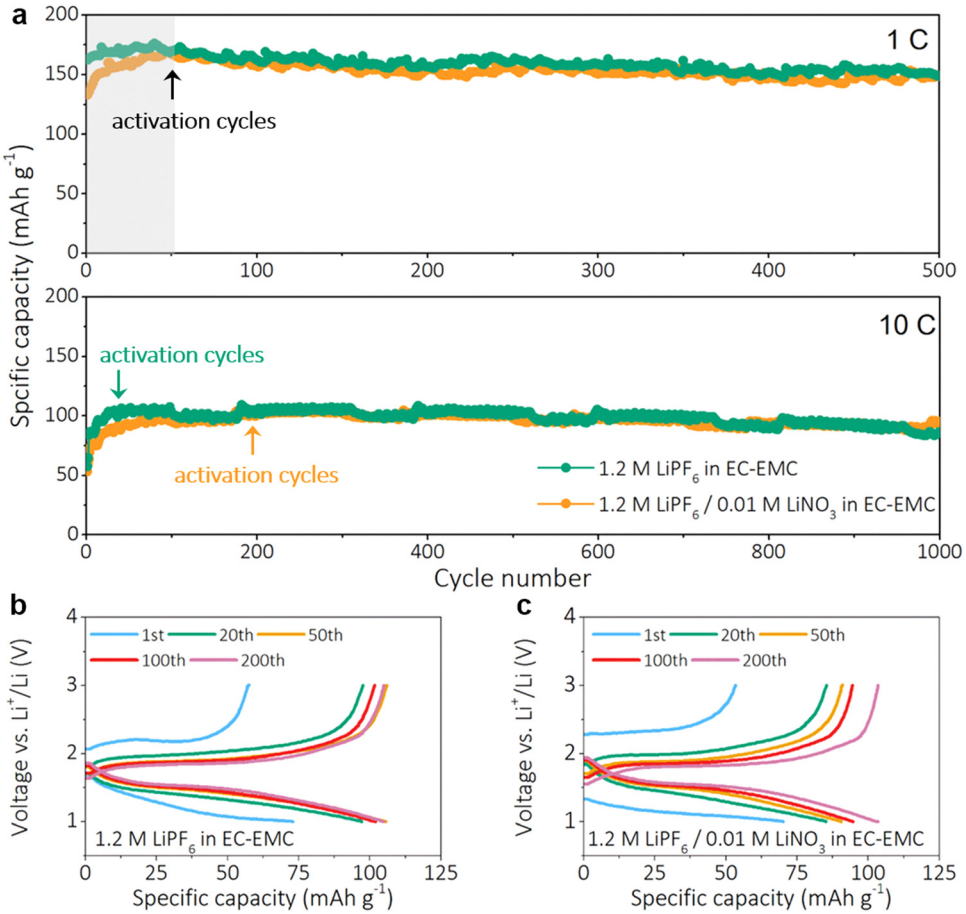

Fig. 5 Electrochemical performance of H-Nb_2O_5 with different SEI structures. (a) Long time cycling performance of H-Nb_2O_5 at 1C and 10C. (b) and (c) Galvanostatic charge and discharge curves (10C) of H-Nb_2O_5 cycled with (b) neat EC-based electrolyte and (c) $LiNO_3$ added EC-based electrolyte for the activation cycles.

the porous SEI is dominant. The pore diffusion means that the lithium ion moves in the liquid electrolyte within the SEI pores, which is much faster than lithium ion diffusion in the solid phase of SEI components (*e.g.*, LiF, Li_2O, Li_2CO_3). The energy barriers of Li ion transport in SEI including Li ion diffusion inside the Li_2O bulk and Li ions hopping in porous dilithium ethylene dicarbonate (Li_2EDC) were compared by density functional theory (DFT) calculations. The pathway of the Li diffusion inside Li_2O with the lowest energy barrier adopts a vacancy diffusion mechanism to adjacent side, which demonstrates an energy barrier of 0.27 eV from initial state to transition state (Fig. 6(c)). In contrast, a much smaller energy barrier of 0.06 eV is obtained for Li ion hopping between two oxygen sites of two EDC ions, which is the major organic product of electrochemical reduction of EC in those EC-based electrolyte.[54] These modeling results illustrate that the Li ions tend to directly pass through the SEI layer without penetrating those discrete Li_2O particles *via* solid state diffusion if there is no dense and complete Li_2O layer formed. In such conditions, the lithium ions tend to directly diffuse across the entire SEI layer in the porous organic components without penetrating through the discrete Li_2O particles. As the result, the kinetic limitation for the lithium transport is mainly controlled by the Li solid diffusion within the host material rather than the Li diffusion through SEI in such a one-step pore diffusion mechanism (Fig. 6(f)).

To further prove such an argument, cryo-STEM images of porous SEI structure with were acquired. While we observed the SEI structures on the Nb_2O_5 particles, the side view images of SEI were only accessed for imaging and spectroscopic analysis, and this makes comprehensive SEI morphology analysis difficult. This is because the presence of large Nb_2O_5 particles blocks electron transparency along electron beam axis. Therefore, we deposited SEI structures on a piece of carbon TEM grid directly without Nb_2O_5 particles to clearly observe top-view morphology (refer to ESI† for details). In the top-view image of the SEI deposited over the carbon grids, we observed that highly porous SEI structures in both electrolytes, no matter if there is $LiNO_3$ or not (Fig. 6(a), (b) and Fig. S13, ESI†). This suggests that although we have different chemistry, thickness, structure in the SEI compositions from the two different electrolytes confirmed by cryo-EELS and cryo-TEM imaging, there are many regions on the surface of Nb_2O_5 particles, accessible to lithium ions in liquid electrolytes without being

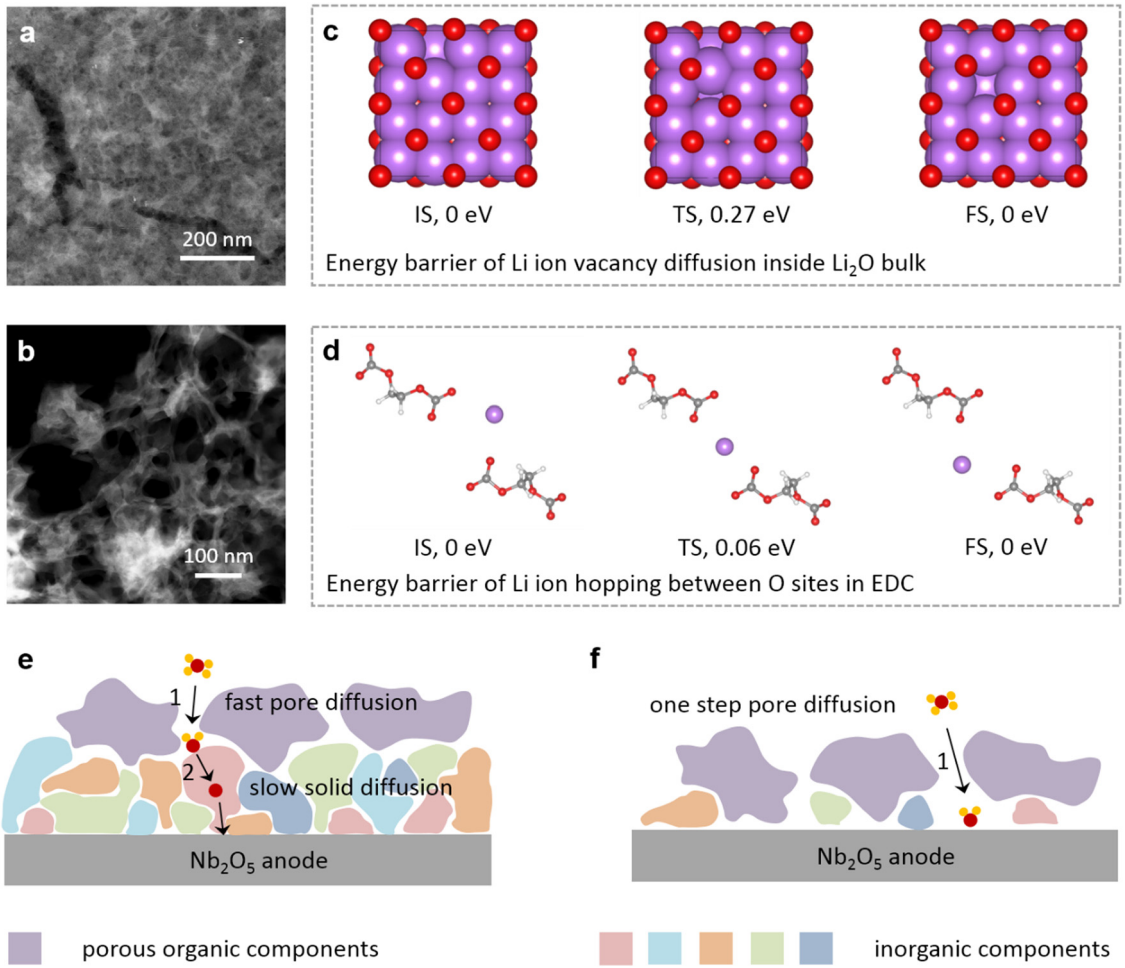

Fig. 6 Mechanism of Li transport pathway across the SEI structures. (a) and (b) HAADF cryo-STEM images of pure porous SEI structure formed in $LiNO_3$ added EC-based electrolyte without Nb_2O_5 particles after 10 cycles in two different magnifications. (c) DFT calculation results of the energy barrier Li ion vacancy diffusion inside the Li_2O bulk from initial state (IS) to transition state (TS) and to final state (FS). (d) The energy barrier of a Li ion hopping between two O sites of two EDC ions. Schematics of typical two step mechanism for Li transport pathway across the SEI (e) and one step pore diffusion mechanism with discrete inorganic particles (f).

blocked by porous SEI, which allows for a fast one-step pore diffusion of lithium ions.

It is notable that the long-term cyclic performance at both 1C and 10C rates are similar no matter what SEI structures were formed on the H-Nb_2O_5 surface of electrode materials. However, the SEI structures from the different electrolytes play a critical role in the activation process (*i.e.*, the beginning cycles). Therefore, EIS measurement was performed to investigate the wetting degree between electrode and electrolyte, which has been found to be highly relevant to the fast-charging capability.[55] The high-frequency resistance (HFR) of the coin cells after different cycles has been used to evaluate this wetting degree.[56] We compared the EIS results with HFR evolution between H-Nb_2O_5 with the SEI-rich and SEI-lean structure and found that there is very little HFR difference ($<0.5\ \Omega$) for those electrodes with different cycles in the electrolyte without $LiNO_3$ additives (Fig. S14, ESI†). However, the HFR continuously decreases from the 1st cycle (8.44 Ω) to the 20th cycle (5.88 Ω) in those H-Nb_2O_5 anode with a SEI-rich structure. These results could be explained by the different evolution of these SEI structures with battery cycles. EC and EMC are quite stable in our battery operating potential range and are only slightly reduced to a direct amorphous thin SEI. In contrast, a continuous propagation of SEI structure is induced by $LiNO_3$ reduction. The stable SEI structure in the EC based electrolyte contributes to a stable wetting between the electrode and the electrolyte, resulting in a shorter activation process. However, the SEI continuously grows until the $LiNO_3$ additives are depleted in the latter case. Those reduction products such as LiN_xO_y and Li_2O may increase the wetting degree and longer cycles of activation are required as a result. Moreover, the continuous growth of the SEI may also lead to a barrier for the pore diffusion process of Li ion transport across the direct SEI. The mechanism of the activation process is still unclear and needs future exploration. But it may be relevant to the formation of the preferential Li conduction pathway in the direct SEI layer for the pore diffusion. Furthermore, the exploration of the activation process with inner H-Nb_2O_5 structure

evolution was evaluated by performing an *ex situ* X-ray diffraction (XRD) after different cycles at 10 C-rate. A typical XRD patterns (PDF#72-1121) of H-Nb_2O_5 are presented for the pristine electrode without cycles (Fig. S15, ESI†). After many cycles of galvanostatic charge/discharge (1–20 cycles), there is no obvious reduction of the peak intensity, indicating that the structural integrity is maintained, regardless of surface SEI structure evolution. These results are consistent with their cycling stability (Fig. 5(a)). The changes in *d*-spacing for two characteristic (110) and (013) peaks further verify that their structural stability, in which less than 0.5% of the *d*-spacing expansion or shrinkage is demonstrated after 20 high-rate cycles for both samples (Table S3, ESI†). These findings further corroborate that the surface structure evolutions (*e.g.*, formation of Li diffusion channels in amorphous organic matrix) account for the discrepancy of the activation process rather than changes to the anode crystalline structure.

To further validate the one-step pore diffusion mechanism in other materials, the rate performance of $Li_4Ti_5O_{12}$ (LTO) anodes were further studied using our EC-based electrolyte combinations. A reduction of ICE from 80.0% to 74.6% was found with $LiNO_3$ additives in the EC-based electrolyte (Fig. S16a, ESI†). The SEI-rich structure is likely to be formed on the LTO surface with $LiNO_3$ added electrolyte considering its same operation potential range as Nb_2O_5 (1.0–3.0 V, *vs.* Li^+/Li). The following rate performance testing validated the superior Li (de)intercalation kinetics in those SEI-rich LTO anodes since a similar specific capacity was observed compared to those LTO cycled in neat EC-based electrolyte (Fig. S16b–d, ESI†). Moreover, the full cells based on Nb_2O_5 anode and $LiFePO_4$ cathode were constructed to evaluate their rate performance at different SEI structures. Due to the addition of $LiNO_3$ in the electrolyte, a much lower ICE (63.9%) is demonstrated compared to the neat EC-based electrolyte (Fig. S17a and b, ESI† 91.0%), corresponding to the irreversible $LiNO_3$ decomposition. This decomposition is similar to the Li/Nb_2O_5 half cells (Fig. 1(b)). At low rate (*e.g.*, 0.1C), the charge/discharge process can be considered as a quasi-thermodynamics equilibrium state, and the specific capacity is mainly controlled by the available amounts of lithium ions for (de)intercalation between anode and cathode. However, after the initial charge process, some of Li ions from $LiFePO_4$ (LFP) are irreversibly consumed to form a SEI-rich structure on the Nb_2O_5 surface, which cannot be retrieved during the discharge process, leading to a reduced capacity called as ''initial capacity loss''.[3] Consequently, those LFP/Nb_2O_5 cells cycled in the $LiNO_3$ added electrolyte suffer from a much lower specific capacity at low rates (0.1C–0.5C, Fig. S17b–d, ESI†) because of the higher initial capacity loss compared to those full cells cycled in neat EC-based electrolyte. However, at the high rate charge/discharge condition (*e.g.*, 1C, and 2C), the specific capacity of the full cell is mainly controlled by the lithium transport kinetics such as the Li transport *via* the SEI and Li diffusion within the LFP or Nb_2O_5. A similar specific capacity of these Nb_2O_5 with different SEI structures in the full cell configurations at high rate condition ($\sim$46 mA h g^{-1}, 2C, Fig. S17b–d, ESI†) suggests a similar SEI kinetic barrier no matter a SEI-lean or SEI-rich structure on Nb_2O_5 surface. These results further prove the viability of our one-step pore diffusion mechanism among different materials and battery configurations.

3. Conclusions

Using $LiNO_3$ as an additive in EC-based electrolyte, we were able to fabricate an SEI-rich layer on H-Nb_2O_5 anode with $LiNO_3$ preferential reduction. The spatial distribution of SEI layer at the surface of H-Nb_2O_5 particles and electrode was examined using cryo-S/TEM and XPS. Our findings indicate that the direct SEI layer on the anode surface is decorated with nano-sized Li_2O crystals and amorphous LiN_xO_y from the decomposition of $LiNO_3$. The electrochemical performance of the SEI-rich anode was compared with those of SEI-lean anode, H-Nb_2O_5 cycled in neat EC-based electrolyte, which only had a much thinner amorphous SEI compared to the SEI from the $LiNO_3$ added electrolyte. Interestingly, both SEI-lean and SEI rich H-Nb_2O_5 anodes demonstrate a similar electrochemical performance including fast-charging capability and cycling stability except for a discrepancy in their activation process. Our results suggest that the thickness of SEI and the presence of specific components (*e.g.*, Li_2O), do not kinetically limit the transport of lithium ions through the SEI layer if an inner inorganic layer is densely not formed. Thus, a one-step pore lithium ion diffusion dominates the transport of lithium ions through the porous organic layer, which is the major component that constitutes the direct SEI layer. This diffusion is extremely fast compared to the solid-state diffusion of lithium ions in the inner H-Nb_2O_5 lattice. Therefore, a similar fast-charging capability is demonstrated regardless of the inorganic components and thickness of the direct organic SEI layer. Such a mechanism is further validated in LTO anode materials and LFP/Nb_2O_5 full cell configurations.

Furthermore, these conclusions provide new findings of the desolvation process. It has been widely accepted that solvated Li ions in the electrolyte must strip its solvation sheath at the interface between the direct SEI and electrolyte, and the SEI layer only allows for the lithium transport of naked Li ions with a solid state diffusion mechanism.[6] However, based on our findings, a pore diffusion of Li ions in liquid state across the porous SEI layer may dominate if the inorganic components are not dense enough. This strongly suggests that the stripping of Li solvation sheath may also happen at the interface between the host materials and the electrolyte within the SEI pore structure. Here is no clear evidence confirms if the new mechanism presented from high voltage H-Nb_2O_5 is also possible in those low voltage anode materials like graphite. However, our new understanding is able to explain previously observed phenomenon which cannot be explained by two-step mechanism, such as the superior rate performance of graphite realized by lithium ions and solvent molecules co-intercalation,[25,28–30,57,58] which further indicate the existence of a similar one-step lithium transport pathway in SEI different from previous accepted two-step mechanism.

Conflicts of interest

The authors declare no competing financial interests.

Acknowledgements

J. X. acknowledges the financial support for the Office of Vice Chancellor for Research (OVCR) *via* the Bridge Funding Program (BRIDGE) and the help from the Post Test Facility at Argonne National Laboratory, supported by the U.S. DOE Vehicle Technologies Office under contract number DE-AC02-06CH11357. H. K. and E. A. S. acknowledge primary financial support from the National Science Foundation (NSF), Division of Materials Research (DMR), Future Manufacturing Research grant #2134715. This work was carried out in part at the Singh Center for Nanotechnology at the University of Pennsylvania, which is supported by the NSF National Nanotechnology Coordinated Infrastructure Program under grant NNCI-2025608. Additional support to the Nanoscale Characterization Facility at the Singh Center has been provided by the Laboratory for Research on the Structure of Matter (MRSEC) supported by the National Science Foundation (DMR-1720530). Z. Z. and A. N. A. acknowledges U.S. DOE, Office of Science, Basic Energy Science Program for financial support under the grant number DE-SC0019152. The computations in this work were performed on Hoffman2, the UCLA-shared cluster. The authors also acknowledge technical assistance from Dr Jamie T. Ford and Dr Douglas M. Yates at Penn.

References

1 P. Verma, P. Maire and P. Novák, *Electrochim. Acta*, 2010, **55**, 6332–6341.
2 E. Peled and S. Menkin, *J. Electrochem. Soc.*, 2017, **164**, A1703.
3 Y. Yu, Z. Yang, Y. Liu and J. Xie, *Carbon*, 2022, **196**, 589–595.
4 B. P. Williams, H. Zhang, Y. Mu, J. R. Wilkes, H. Wikar and D. Wang, *J. Phys. Chem. C*, 2022, **126**, 10644–10652.
5 X. B. Cheng, R. Zhang, C. Z. Zhao and Q. Zhang, *Chem. Rev.*, 2017, **117**, 10403–10473.
6 W. Cai, Y.-X. Yao, G.-L. Zhu, C. Yan, L.-L. Jiang, C. He, J.-Q. Huang and Q. Zhang, *Chem. Soc. Rev.*, 2020, **49**, 3806–3833.
7 S. Shi, P. Lu, Z. Liu, Y. Qi, L. G. Hector Jr, H. Li and S. J. Harris, *J. Am. Chem. Soc.*, 2012, **134**, 15476–15487.
8 F. A. Soto, A. Marzouk, F. El-Mellouhi and P. B. Balbuena, *Chem. Mater.*, 2018, **30**, 3315–3322.
9 X. Lou, R. Li, X. Zhu, L. Luo, Y. Chen, C. Lin, H. Li and X. Zhao, *ACS Appl. Mater. Interfaces*, 2019, **11**, 6089–6096.
10 Q. Fu, X. Liu, J. Hou, Y. Pu, C. Lin, L. Yang, X. Zhu, L. Hu, S. Lin and L. Luo, *J. Power Sources*, 2018, **397**, 231–239.
11 W. Zhang, D.-H. Seo, T. Chen, L. Wu, M. Topsakal, Y. Zhu, D. Lu, G. Ceder and F. Wang, *Science*, 2020, **367**, 1030–1034.
12 H. Sun, L. Mei, J. Liang, Z. Zhao, C. Lee, H. Fei, M. Ding, J. Lau, M. Li and C. Wang, *Science*, 2017, **356**, 599–604.
13 B. Guo, X. Yu, X.-G. Sun, M. Chi, Z.-A. Qiao, J. Liu, Y.-S. Hu, X.-Q. Yang, J. B. Goodenough and S. Dai, *Energy Environ. Sci.*, 2014, **7**, 2220–2226.
14 K. J. Griffith, K. M. Wiaderek, G. Cibin, L. E. Marbella and C. P. Grey, *Nature*, 2018, **559**, 556–563.
15 K. J. Griffith, A. C. Forse, J. M. Griffin and C. P. Grey, *J. Am. Chem. Soc.*, 2016, **138**, 8888–8899.
16 M. A. Reddy and U. Varadaraju, *J. Phys. Chem. C*, 2011, **115**, 25121–25124.
17 J.-T. Han and J. B. Goodenough, *Chem. Mater.*, 2011, **23**, 3404–3407.
18 X. Cao, X. Ren, L. Zou, M. H. Engelhard, W. Huang, H. Wang, B. E. Matthews, H. Lee, C. Niu and B. W. Arey, *Nat. Energy*, 2019, **4**, 796–805.
19 J. Zheng, M. H. Engelhard, D. Mei, S. Jiao, B. J. Polzin, J.-G. Zhang and W. Xu, *Nat. Energy*, 2017, **2**, 17012.
20 Z. Tu, S. Choudhury, M. J. Zachman, S. Wei, K. Zhang, L. F. Kourkoutis and L. A. Archer, *Nat. Energy*, 2018, **3**, 310–316.
21 A. Ghosh and F. Ghamouss, *Front. Mater.*, 2020, **7**, 186.
22 H. Jin, S. Xin, C. Chuang, W. Li, H. Wang, J. Zhu, H. Xie, T. Zhang, Y. Wan and Z. Qi, *Science*, 2020, **370**, 192–197.
23 H. Liu, Z. Zhu, Q. Yan, S. Yu, X. He, Y. Chen, R. Zhang, L. Ma, T. Liu and M. Li, *Nature*, 2020, **585**, 63–67.
24 N. Kim, S. Chae, J. Ma, M. Ko and J. Cho, *Nat. Commun.*, 2017, **8**, 1–10.
25 H. Kim, K. Lim, G. Yoon, J. H. Park, K. Ku, H. D. Lim, Y. E. Sung and K. Kang, *Adv. Energy Mater.*, 2017, **7**, 1700418.
26 B. Jache and P. Adelhelm, *Angew. Chem., Int. Ed.*, 2014, **53**, 10169–10173.
27 L. Li, L. Liu, Z. Hu, Y. Lu, Q. Liu, S. Jin, Q. Zhang, S. Zhao and S. L. Chou, *Angew. Chem., Int. Ed.*, 2020, **59**, 12917–12924.
28 H. Kim, J. Hong, Y. U. Park, J. Kim, I. Hwang and K. Kang, *Adv. Funct. Mater.*, 2015, **25**, 534–541.
29 A. P. Cohn, N. Muralidharan, R. Carter, K. Share, L. Oakes and C. L. Pint, *J. Mater. Chem. A*, 2016, **4**, 14954–14959.
30 J. Ming, Z. Cao, W. Wahyudi, M. Li, P. Kumar, Y. Wu, J.-Y. Hwang, M. N. Hedhili, L. Cavallo, Y.-K. Sun and L.-J. Li, *ACS Energy Lett.*, 2018, **3**, 335–340.
31 Y. Liu, D. Lin, Y. Li, G. Chen, A. Pei, O. Nix, Y. Li and Y. Cui, *Nat. Commun.*, 2018, **9**, 1–10.
32 D. Liu, X. Xiong, Q. Liang, X. Wu and H. Fu, *Chem. Commun.*, 2021, **57**, 9232–9235.
33 S. J. An, J. Li, C. Daniel, D. Mohanty, S. Nagpure and D. L. Wood, *Carbon*, 2016, **105**, 52–76.
34 S. S. Zhang, *J. Electrochem. Soc.*, 2012, **159**, A920.
35 H. Liu, Z. Bi, X. G. Sun, R. R. Unocic, M. P. Paranthaman, S. Dai and G. M. Brown, *Adv. Mater.*, 2011, **23**, 3450–3454.
36 D. Lee, H. Park, A. Goliaszewski, Y.-K. Byeun, T. Song and U. Paik, *Ind. Eng. Chem. Res.*, 2019, **58**, 8123–8130.
37 C. Yan, Y. X. Yao, X. Chen, X. B. Cheng, X. Q. Zhang, J. Q. Huang and Q. Zhang, *Angew. Chem., Int. Ed.*, 2018, **130**, 14251–14255.
38 W. Huang, H. Wang, D. T. Boyle, Y. Li and Y. Cui, *ACS Energy Lett.*, 2020, **5**, 1128–1135.

39 Y. Li, Y. Li, A. Pei, K. Yan, Y. Sun, C.-L. Wu, L.-M. Joubert, R. Chin, A. L. Koh and Y. Yu, *Science*, 2017, **358**, 506–510.
40 M. J. Zachman, Z. Tu, S. Choudhury, L. A. Archer and L. F. Kourkoutis, *Nature*, 2018, **560**, 345–349.
41 J. L. White, A. A. Baker, M. A. Marcus, J. L. Snider, T. C. Wang, J. R. Lee, D. A. Kilcoyne, M. D. Allendorf, V. Stavila and F. El Gabaly, *Adv. Mater. Interfaces*, 2020, **7**, 1901905.
42 Z. Zhang, J. Yang, W. Huang, H. Wang, W. Zhou, Y. Li, Y. Li, J. Xu, W. Huang and W. Chiu, *Matter*, 2021, **4**, 302–312.
43 F. Lin, I. M. Markus, M. M. Doeff and H. L. Xin, *Sci. Rep.*, 2014, **4**, 1–6.
44 C. Funke and V. S. K. Chakrvadhanula, *Phys. Sci. Rev.*, 2018, **4**, 20170153.
45 L. Lodovico, A. Varzi and S. Passerini, *J. Electrochem. Soc.*, 2017, **164**, A1812.
46 E. J. McShane, H. K. Bergstrom, P. J. Weddle, D. E. Brown, A. M. Colclasure and B. D. McCloskey, *ACS Energy Lett.*, 2022, **7**, 2734–2744.
47 C. Y. Kim, G. H. Lee, H. A. So, K. H. Shin and Y. J. Lee, *ACS Appl. Mater. Interfaces*, 2020, **12**, 49541–49548.
48 Z. Song, H. Li, W. Liu, H. Zhang, J. Yan, Y. Tang, J. Huang, H. Zhang and X. Li, *Adv. Mater.*, 2020, **32**, 2001001.
49 T. Li, G. Nam, K. Liu, J.-H. Wang, B. Zhao, Y. Ding, L. Soule, M. Avdeev, Z. Luo and W. Zhang, *Energy Environ. Sci.*, 2022, **15**, 254–264.
50 Y. Yu, Y. Liu and J. Xie, *ACS Appl. Mater. Interfaces*, 2021, **13**, 18–33.
51 O. Borodin, G. V. Zhuang, P. N. Ross and K. Xu, *J. Phys. Chem. C*, 2013, **117**, 7433–7444.
52 L. Benitez and J. M. Seminario, *J. Electrochem. Soc.*, 2017, **164**, E3159.
53 Z. Liu, W. Dong, J. Wang, C. Dong, Y. Lin, I.-W. Chen and F. Huang, *iScience*, 2020, **23**, 100767.
54 G. V. Zhuang, K. Xu, H. Yang, T. R. Jow and P. N. Ross, *J. Phys. Chem. B*, 2005, **109**, 17567–17573.
55 D. S. Kim, Y. E. Kim and H. Kim, *J. Power Sources*, 2019, **422**, 18–24.
56 F. J. Günter, J. B. Habedank, D. Schreiner, T. Neuwirth, R. Gilles and G. Reinhart, *J. Electrochem. Soc.*, 2018, **165**, A3249.
57 L. Li, L. Liu, Z. Hu, Y. Lu, Q. Liu, S. Jin, Q. Zhang, S. Zhao and S. L. Chou, *Angew. Chem., Int. Ed.*, 2020, **59**, 12917–12924.
58 B. Jache and P. Adelhelm, *Angew. Chem., Int. Ed.*, 2014, **126**, 10333–10337.